J. Fluid Mech. (1975), *vol.* 67, *part* 1, *pp.* 65–84
Printed in Great Britain

Stability characteristics of a single-phase free convection loop

By H. F. CREVELING,† J. F. DE PAZ, J. Y. BALADI AND R. J. SCHOENHALS
Purdue University, West Lafayette, Indiana

(Received 10 January 1973 and in revised form 15 June 1974)

Stability characteristics of a single-phase free convection loop are presented. In the experiments, water was placed inside a toroidal glass loop oriented in a vertical plane. The lower half of the loop was heated and the upper half was cooled. At low heat-transfer rates and also at high heat-transfer rates the free convection flow was observed to be steady. For the intermediate range, however, the flow was found to be highly oscillatory. Stability predictions are also developed. The comparison between theory and experiment yields favourable agreement.

Observations of unstable behaviour have been reported previously for single-phase fluids in the vicinity of the thermodynamic critical point. In these situations it has been assumed that the unusual behaviour of the fluid properties in the near-critical region necessarily constitutes the underlying cause of such instabilities. In contrast to this view, analyses by Keller (1966) and Welander (1967) indicate that instabilities can occur for ordinary fluids as well. Results of the present study confirm this contention, since instabilities were clearly observed for water at atmospheric pressure and moderate temperatures.

1. Introduction

Fluid flow in a free convection loop (figure 1) is created by buoyancy forces as a result of differences in fluid density induced by temperature variations. Fluid in the vicinity of the sink is cooled, becomes more dense and therefore tends to move downwards. Conversely, fluid in the vicinity of the source is heated, becomes lighter and rises upwards on the right side of the loop. The fluid temperature distribution and the associated buoyancy force driving the flow are dependent upon the flow rate, as is the frictional retarding force. With the heating and cooling conditions at the source and sink maintained constant, an initially stationary fluid would be expected to accelerate until the buoyancy and frictional effects become equal, thus yielding a steady state of constant flow rate thereafter. However, there are circumstances in which a steady state cannot be achieved. In these situations an unstable oscillatory flow occurs instead. The existence of this phenomenon is well known in the case of two-phase fluids. For single-phase

† Present address: Detroit Diesel Allison Division, General Motors Corporation, Indianapolis, Indiana.

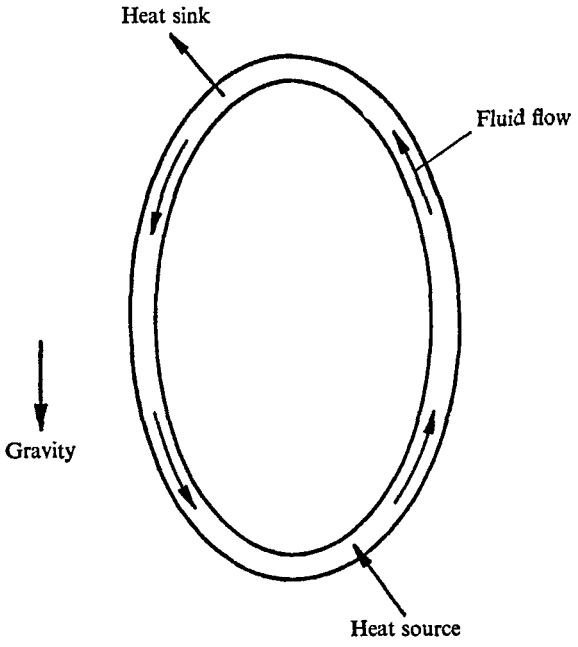

FIGURE 1. Free convection loop.

fluids, which are the concern of this paper, observations of instabilities have been previously reported only for fluids operating in the vicinity of the thermodynamic critical point.

The earliest reported observation of free convection instability for a near-critical fluid was made by Schmidt, Eckert & Grigull (1939) using pressurized ammonia. This unexpected behaviour was later observed for other near-critical fluids in free convection loops, first by Holman & Boggs (1960) for Freon-12 and then by Van Putte (1961) for water. In each of these instances an experimental study of the flow and heat-transfer performance was pursued, the instability being encountered incidentally.

Harden (1963) and Cornelius (1965) specifically studied instabilities of near-critical Freon-114 in free convection loops. Two frequency ranges were found, the higher frequencies apparently being associated with the propagation of sonic waves in the fluid. Finite-difference calculations based on the conservation equations also exhibited instabilities, and these were correlated with the observed oscillations in the lower frequency range.

The references cited above treat only instabilities encountered in the vicinity of the critical point. In each of these cases it was assumed that the instability was caused by the large fluid-property variations in this region. The existence of such instabilities for ordinary fluids at moderate pressures did not appear likely. Further, Alstad *et al.* (1956) measured the transient response of a free convection loop containing ordinary water and did not observe any instabilities. However, Keller (1966) and Welander (1967) have shown analytically that loop flow instabilities are predicted by the dynamics of the system, without consideration

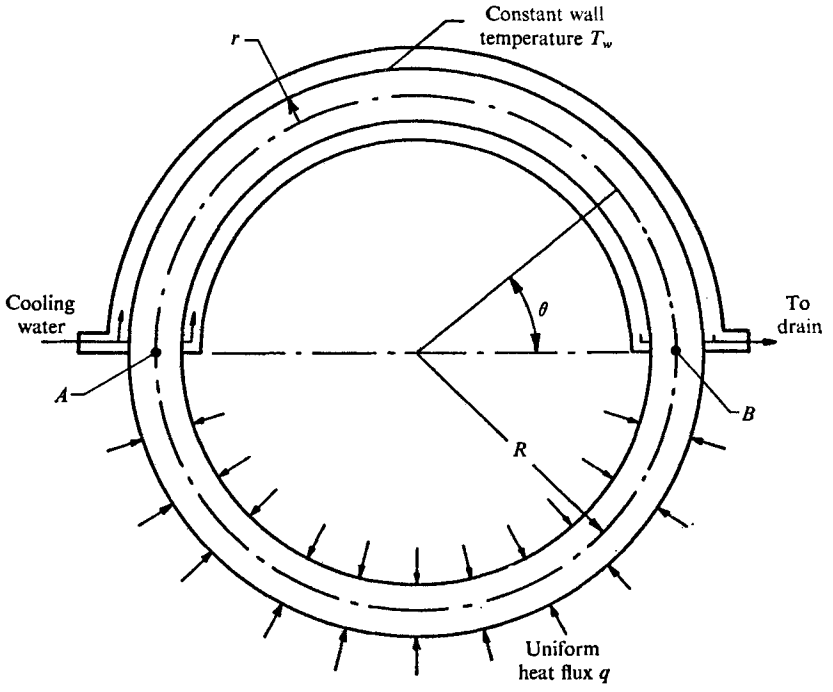

FIGURE 2. Free convection loop employed for experimental study (R = 38 cm, r = 1·5 cm).

of unusual fluid-property behaviour. On the basis of these analyses instabilities should exist under certain conditions for ordinary fluids, as well as near-critical fluids, even though one may not intuitively expect them. To the knowledge of the authors, no experiments have been reported previously which exhibit the instability for an ordinary fluid at moderate pressures and temperatures. Since the existence of these instabilities has been predicted analytically, it appears appropriate to provide an experimental confirmation. This is the primary purpose of the present paper, which reports observation of instabilities for a loop containing water at a pressure of one atmosphere and at moderate temperatures. In addition, it is shown that a stability analysis of the system yields predictions which are in agreement with the experiments.

2. Experimental apparatus

A loop of circular geometry was chosen for this study; figure 2 shows the essential features. This system allowed for distributed heating and cooling, and was also tractable to analysis. Water circulated inside the toroidal loop, which was made of Pyrex glass. A concentric cooling jacket of the same material surrounded the upper half of the torus, while heat was supplied to the lower half by means of two ribbon-type heating elements connected to a variable electrical power supply. An autotransformer was used to supply electrical power. The ribbon was tightly wound on the glass with the windings close together in an

attempt to approach a constant-heat-flux condition at the wall. The power supplied to the windings was measured with a wattmeter. The lower half of the loop was wrapped on the outside with glass-wool insulation to minimize heat losses.

Tap water was supplied to the cooling jacket through a flowmeter, and its temperature was measured with precision thermometers placed upstream and downstream of the cooling jacket in order to provide a measurement of the heat flow from the system to the coolant. The coolant flow rate was large enough so that the tube wall was essentially at a uniform temperature only slightly above the temperature of the coolant. The interior of the loop was connected by a tube to an open reservoir to maintain it essentially at atmospheric pressure. The cooler section of the torus was left uncovered to allow visual observation of the flow. The loop was filled with distilled water.

Two copper–constantan thermocouples were inserted inside the loop at the ends of the heater section (points A and B in figure 2) to monitor the temperature of the interior fluid. The thermocouples were placed at a distance from the wall 0·45 times the inner tube radius. This corresponds to the position at which the local fluid temperature is equal to the bulk temperature for a conventional fully developed laminar profile. Although the conditions inside the loop were not expected to conform closely to those of the fully developed laminar regime, this position was adopted for lack of better information. For turbulent flow the temperature profile can be expected to be quite flat, so that the exact position of the probe is not very critical. The thermocouple wires were connected to provide measurements of the water temperature at one end of the heated section (point A) and also the temperature difference across the heated section (points A and B). A strip-chart recorder provided continuous plots of these signals.

3. Experimental observations

At the start of each test there was no flow inside the loop, the water in the lower half being heated and that in the upper half being cooled. For this initial condition local heat convection and conduction occurred owing to the large temperature gradients at sections A and B. This condition was unstable and gave way to a flow under any disturbance, and the water began to flow in one direction or the other. For initial motion in the counterclockwise direction cold water moved across section A and hot water moved across section B. This produced sizeable density gradients in both halves of the loop, and the resulting buoyancy force accelerated the flow. The temperature and density gradients were moderated as the flow rate increased, and this caused the buoyancy driving force to decrease. Simultaneously, frictional resistance to the motion increased. In some cases, steady-state conditions were finally achieved when the buoyancy driving force and frictional force became equal. In other cases, as noted in § 1, the flow failed to reach a steady state and oscillated indefinitely. Thus, both stable and unstable flow behaviour were observed in the present study when the electrical heat input, coolant flow rate and coolant inlet temperature were maintained constant.

In the case of stable operation any disturbance was observed to damp out as

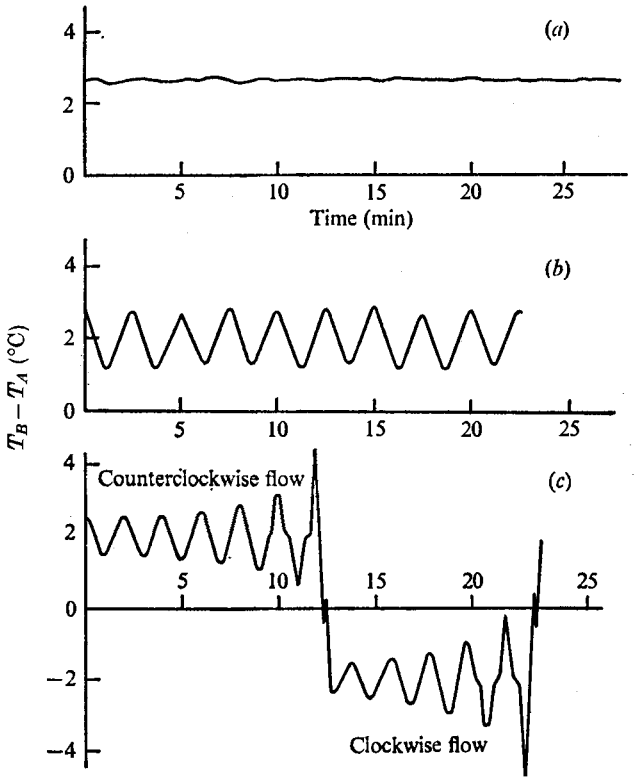

FIGURE 3. Fluctuations in the temperature difference between sections A and B. (a) Stable flow, (b) neutrally stable flow, (c) unstable flow.

the circulation flow rate became constant. In the case of unstable operation the fluid temperatures were observed to fluctuate with sizeable amplitudes, indicating variations in the flow rate. In typical unstable situations the flow rate not only oscillated, but reversed direction as well. Between the stable and unstable regimes there was observed to be a condition under which the temperatures exhibited sustained fluctuations of approximately constant amplitude. This condition is classified as neutrally stable. Figure 3 illustrates various forms of observed recordings of the temperature difference between sections A and B for different flow conditions. In the case of the stable flow situation shown, T_B is greater than T_A, indicating flow in the counterclockwise direction. Conversely, clockwise flow was detected when T_B was observed to be smaller than T_A. Notice that the unstable flow case shown exhibits a flow reversal, from counterclockwise to clockwise motion, as evidenced by a change in the sign of the recorded temperature difference, from positive to negative.

It was observed that the amplitude of the oscillation kept increasing until the temperature-difference curve passed through zero. This was associated with a reversal of the flow. In the unstable situation depicted in figure 3 the time-averaged flow is counterclockwise during the initial stage of amplification. This is followed by a second stage of amplification, during which the time-averaged flow is clockwise, and the counterclockwise time-averaged flow appears once

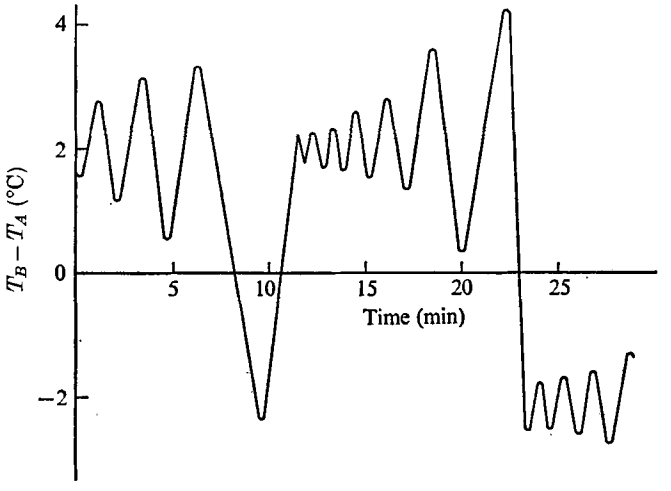

FIGURE 4. Fluctuations in the temperature difference between sections A and B exhibiting reversion to original flow direction after a flow reversal.

again during the third stage. Thus, the time-averaged flow alternates indefinitely between clockwise and counterclockwise, with the actual flow oscillating during each of these stages about the time-averaged value. However, in most cases there was not a regular periodicity of the time-averaged flow as characterized by the unstable situation illustrated in figure 3. In these instances (see figure 4) a particular flow reversal was not necessarily followed by an amplification stage in the reversed flow direction. Instead the flow, after reversing, would immediately revert back to the original flow direction and this would be followed by another amplification stage until the next flow reversal occurred. At that point the flow might revert back immediately to the original flow direction, as in the previous reversal, or this might be followed by an amplification in the reversed flow direction as shown in figure 4. In all unstable situations the flow changed alternately between clockwise and counterclockwise, with each reversal being followed by either a sustained stage of amplification or a reversion to the previous flow direction. The flow reversals indicated by sign changes in the temperature difference (figures 3 and 4) were verified by visual observation of the motions of small particles suspended in the circulating water. These could be viewed easily in the uncovered upper portion of the glass loop.

It is interesting to note that, on the basis of analysis, Keller (1966) describes unstable conditions in which the flow oscillates while always moving in the same direction. This description compares favourably with the oscillations observed during each amplification stage as shown in figures 3 and 4, but does not account for the observed flow reversals. On the other hand the 'numerical experiments' of Welander (1967), based on a finite-difference analysis, did show flow reversals similar to those exhibited by the experimental apparatus of the present study (figures 3 and 4). These comparisons are considered significant despite differences in the systems investigated. Keller and Welander studied rectangular loops with straight vertical conduits and with heating and cooling over small discrete sections at the bottom and top, whereas the apparatus used in this investigation was

circular and incorporated distributed heating and cooling sections. This choice was made since distributed heating and cooling could be readily obtained; short discrete sections would have provided far less capacity experimentally. Also, Creveling (1964) had obtained preliminary stability predictions for the circular loop, and it was therefore desired to pursue this case further.

It was found that there were two ranges of heat input in which the system was stable: a low heat input range in which the flow appeared laminar, and a high heat input range which was accompanied by turbulent flow. At intermediate values of the heating the flow was found to be unstable. The boundaries of this region of instability were found to be approximately 0·11 and 0·70 W/cm^2. The frequency of the oscillations increased from 0·007 to 0·018 Hz as the heat input was increased within the unstable range. In each case the period of oscillation was found to be approximately equal to the time required for an element of fluid to circulate once around the loop.

It was observed that when a change in heating was imposed to cause a transition from a stable steady state into an unstable situation, the oscillations developed very gradually and the flow reversals did not start until a considerable time had elapsed. A similar phenomenon occurred during the transition from unstable to stable conditions, in which case the oscillations did not subside until a considerable time had elapsed after the change in input heating. In some cases the waiting periods were approximately 2 h. Several series of experiments were conducted at both progressively increasing and decreasing heating levels. The transitions between steady and unsteady flows were found to occur at the two values of the heating given above regardless of whether the heating rate was being increased or decreased.

During the turbulent tests fast and fairly uniform eddies moving in the direction of the bulk flow were observed in the fluid. But occasionally, near the inlet to the cooled section, some eddies moved in the opposite direction, that is, towards the heated section. This indicated that, in a small region at the beginning of the cooled section, the fluid velocity at the wall was opposite to the bulk movement of the flow, undoubtedly owing to the rapid cooling and increase in density of the fluid near the wall.

At this point it is appropriate to inquire about the physical cause of the observed instability. As discussed by Welander (1967), it appears at first glance that the system should always be stable. The argument is that an increase in flow rate above the steady-state value produces a corresponding increase in friction and a decrease in total buoyancy. The net effect is to retard the flow, thus tending to return the system to the original steady state. A decrease in flow produces the opposite effect. According to this argument the system is self-correcting under any flow disturbance, thus leading to the expectation that the system should always be stable.

Obviously the system can be unstable, so the above explanation based on simple intuitive reasoning is incomplete. Welander has provided a plausible argument to explain the unstable situation. First, consider the system to be operating in a steady state. Then, if a small thermal disturbance causes a 'pocket' of fluid to emerge from the heated section slightly hotter than is normal for this

steady state, the total buoyancy is momentarily increased and the flow accelerates slightly. This hotter-than-normal 'pocket' therefore proceeds through the cooled section more rapidly than normal, and is warmer than normal as it leaves the cooler. The total buoyancy is therefore decreased, decelerating the flow. Thus, the 'pocket' enters the heated section once more, but at a higher inlet temperature and at a lower velocity. These two effects combined cause the pocket to emerge from the heater still hotter than before. This explanation is in accord with the observed build-up of temperature oscillations during periods of amplification as shown in figures 3 and 4. It is also in agreement with the observation from the present study that the period of oscillation is approximately equal to the time required for an element of fluid to circulate once around the loop. Following the same kind of logic for a pocket of fluid which initially emerges from the heater cooler than normal leads to the same oscillatory result. This line of reasoning can also be extended to provide a plausible explanation for the observed flow reversal which occurs at the end of each amplification stage. This physical description is discussed here since the mathematical stability analyses given by Keller and Welander and that given in § 5 of this paper do not seem to yield a vivid physical picture of how the instability is generated. The analysis is successful, however, in predicting the range of conditions in which this phenomenon occurs.

4. Evaluation of system operation

An energy balance was made for each test to evaluate the magnitude of the heat exchange with the environment. To do this, the electrical power input was compared with the rate at which energy was removed by the water in the cooling jacket. Heat removal was calculated from the measured mass flow rate of the cooling water and the difference in the coolant temperatures at either end of the jacket. Except for the experiments with the lowest heat fluxes, the energy removed by the coolant was found to be different from the heater input by less than 10 %, thus providing an indication of the extent of heat exchange with the environment.

The mass flux G inside the loop was calculated from an energy balance across the heated section. Hence,

$$G = Q/\pi r^2 C \Delta T, \tag{1}$$

where C is the specific heat of the fluid, Q the rate of electrical heat input and ΔT the temperature increase of the fluid across the heater. Heat loss to the environment and heat conduction through the ground glass joints between the heated and cooled sections were neglected in these calculations. For the unstable runs ΔT was taken to be the average of the oscillatory response recorded (figures 3 and 4). The input heat flux q was computed from

$$q = Q/2\pi^2 rR. \tag{2}$$

Values calculated from (1) and (2) provided the experimental values of the mass flux as a function of heat flux for the system. A plot of these data is compared with the corresponding analytical prediction in § 5; the results show that G increases with q as expected.

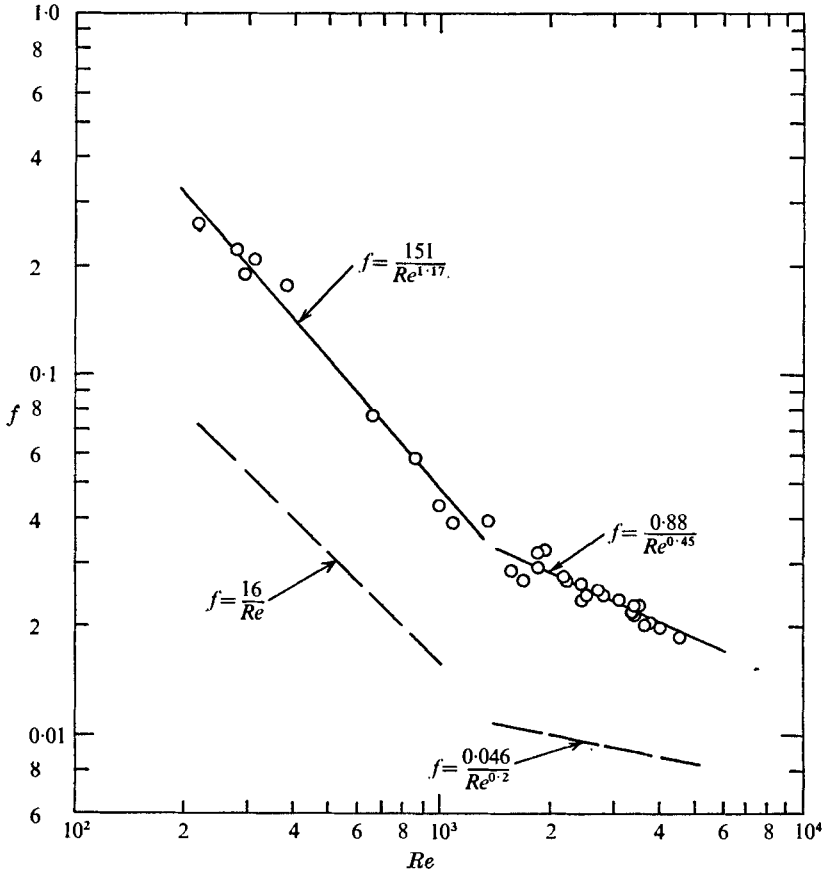

FIGURE 5. Effect of Reynolds number on friction factor.

For purposes of analysis correlations for the friction factor and Nusselt number were needed. It was determined experimentally that standard correlations are greatly in error for flows in free convection loops. Therefore, toroidal-loop correlations were developed using experimental measurements. The rationale employed in constructing these correlations was based on a consideration of steady-state conditions only.

From the analysis in § 5 the friction factor f can be expressed in terms of G and q according to

$$f = 4gR\rho_0^2\beta q/\pi CG^3, \tag{3}$$

where g is the acceleration due to gravity, β is the thermal expansion coefficient and ρ_0 is a reference fluid density. For each calculated value of G the Reynolds number $Re = 2rG/\mu$ can be evaluated. If the calculated values of f and Re are plotted in logarithmic co-ordinates, a straight-line fit to this plot yields the values of a and b for a friction-factor correlation of the form $f = a/Re^b$. This is shown in figure 5. The trend defined by the data points exhibits a slope change for Re approximately equal to 1500, indicating the region of transition between the

laminar and turbulent regimes. The straight lines shown are those giving a least-squares fit to the data points. The resulting correlations are

$$f = 151/Re^{1\cdot17} \tag{4}$$

for laminar flow and

$$f = 0\cdot88/Re^{0\cdot45} \tag{5}$$

for turbulent flow. Note from figure 5 that the experimentally determined values of f are somewhat higher than those predicted by the standard correlations for forced flow in a tube.

As in the case of the friction factor, experimentally determined values of the heat-transfer coefficient in the upper portion of the loop were found to be considerably higher than those obtained from the standard forced convection correlations for flow in a tube. This agrees with the conclusion of Holman & Boggs (1960), who observed similar deviations for free convection loop flow. To alleviate the problem a correlation for the Nusselt number was generated experimentally on the basis of the development below.

The heat-transfer rate to the cooling jacket is expressed as $h2\pi^2rR(T_b - T_w)_{\mathrm{av}}$, where h is the heat-transfer coefficient and $(T_b - T_w)_{\mathrm{av}}$ is the average difference between the bulk fluid and wall temperatures. This heat flow is balanced by the net convective flow corresponding to the temperature difference between points A and B in figure 2, and this difference also provides a measure of the buoyancy torque about the centre of the loop. For the purpose of establishing the functional form of the correlation, a simplified approximation for the buoyancy torque can be written down in terms of this temperature difference. This approximate torque, when set equal to the opposing frictional torque for steady flow, leads to

$$\frac{NuGr}{Pr}\frac{R}{r} = aRe^{3-b}, \tag{6}$$

where Pr is the Prandtl number, the Nusselt number Nu is defined as $2rh/k$ (k being the thermal conductivity of the fluid) and the Grashof number Gr is defined as $g(2r)^3\beta\rho^2(T_b - T_w)_{\mathrm{av}}/\mu^2$. The form of the correlation given in (6) is appropriate to the actual system. However, values of the constants a and b obtained from (4) and (5) are somewhat in error in (6), as expected, owing to the approximations used in this simplified derivation. Hence, the form of (6) is retained at this point, but a is replaced by a different constant m, and the exponent $3-b$ is replaced by a different constant n. Thus,

$$\frac{NuGr}{Pr}\frac{R}{r} = mRe^{n}. \tag{7}$$

The left-hand side of (7) contains only fluid properties, system dimensions, and the product of h and $(T_b - T_w)_{\mathrm{av}}$, which is the average heat flux at the surface of the cooled section. The latter is easily calculated by dividing the measured heat input rate by the surface area of the cooler. Thus, a numerical value of

$$\frac{NuGr}{Pr}\frac{R}{r}$$

was calculated for each test. As described previously, a calculated value of Re was also obtained for each test. Values of $(NuGr/Pr)(R/r)$ and Re, as obtained from

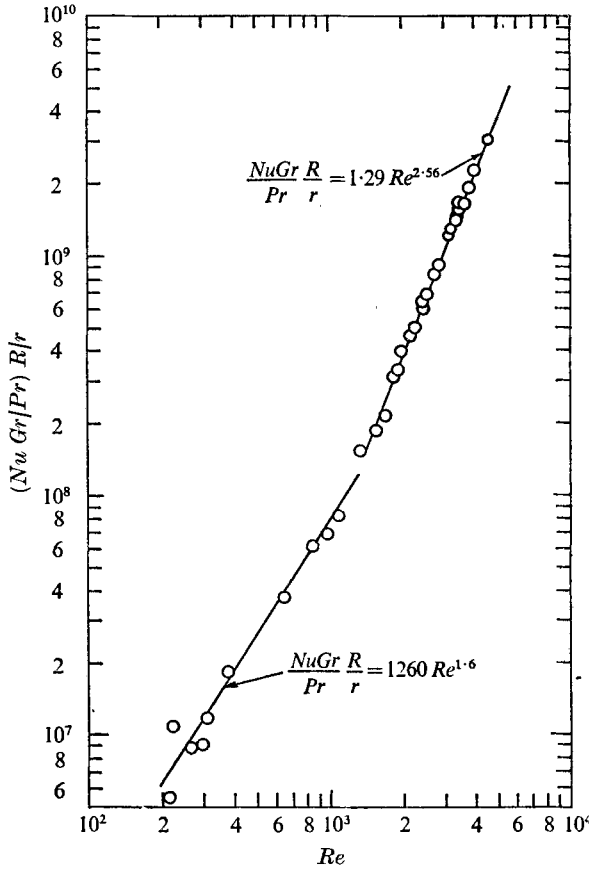

FIGURE 6. Effect of Reynolds number on heat-transfer parameter.

the experiments, are plotted in logarithmic co-ordinates in figure 6. Two straight lines were fitted to the data points by the method of least squares. The resulting correlations are

$$\frac{NuGr}{Pr}\frac{R}{r} = 1260Re^{1{\cdot}6} \tag{8}$$

for laminar flow and

$$\frac{NuGr}{Pr}\frac{R}{r} = 1{\cdot}29Re^{2{\cdot}56} \tag{9}$$

for the turbulent regime. Note that the data in figure 6 follow a well-defined trend with little scatter. This confirms the validity of the form of (7).

Equations (4), (5), (8) and (9) make it possible to determine analytically, for each value of the input heating rate, the steady-state flow and temperature distribution, and whether the steady-state solution is stable or unstable. This analytical development now follows.

5. Comparison with theory

Since the apparatus used in this study was different from those analysed by Keller (1966) and Welander (1967), an analysis of the system (figure 2) is required to provide a detailed comparison of observations with theory. It is considered that the system is subjected to a uniform heat flux over the internal area of its lower half and is cooled by applying a constant wall temperature over the entire internal area of its upper half. For simplicity, a one-dimensional analysis is performed. Axial heat conduction and viscous heating are neglected, and fluid properties are considered constant except for the effect of density variations in producing buoyancy. For this purpose density is related to temperature according to $\rho = \rho_0[1-\beta(T-T_0)]$, where ρ_0 is a nominal value of the density corresponding to a reference temperature T_0. For convenience, T_0 is taken to be the cooler wall temperature, T_w. The conservation equations are

$$\frac{\partial \rho}{\partial t}+\frac{1}{R}\frac{\partial(\rho V)}{\partial \theta}=0, \tag{10}$$

$$\rho C\left[\frac{\partial T}{\partial t}+\frac{V}{R}\frac{\partial T}{\partial \theta}\right]=\begin{cases}(2h/r)(T_w-T) & \text{for} \quad 0<\theta<\pi,\\ (2/r)q & \text{for} \quad \pi<\theta<2\pi,\end{cases} \tag{11}$$

$$\frac{\partial(\rho V)}{\partial t}+\frac{1}{R}\frac{\partial(\rho V^2)}{\partial \theta}=-\frac{1}{R}\frac{\partial p}{\partial \theta}-\rho g\cos\theta-\frac{2}{r}\tau_w. \tag{12}$$

For steady-state conditions (10) indicates that the mass flux ρV is constant along the loop. Integrating (12) around the loop gives

$$g\int_0^{2\pi}\rho\cos\theta\,d\theta+\frac{2}{r}\int_0^{2\pi}\tau_w d\theta=0, \tag{13}$$

which shows the balance between buoyancy and friction. By definition the wall shear stress is expressed as $\tau_w=\frac{1}{2}f\rho V^2$, where f is correlated by $f=a/Re^b$ according to the experimental evaluation described in § 4. τ_w can therefore be written as $a\mu^b G^{2-b}/2^{b+1}r^b\rho$. This is inserted into (13) and the buoyancy term is expressed in terms of T to give

$$g\rho_0\beta\int_0^{2\pi}T\cos\theta\,d\theta-\frac{a\mu^b G^{2-b}}{2^b r^{b+1}}\frac{2\pi}{\rho_0}=0. \tag{14}$$

Integration of (11) for steady-state conditions leads to two expressions for $T(\theta)$ for the heated and cooled sections, respectively. Imposing continuity conditions $T(0)=T(2\pi)$ and $T(\pi^-)=T(\pi^+)$ leads to

$$T=\begin{cases}T_w+\dfrac{A}{\beta}\dfrac{e^{AB}}{e^{AB}-1}e^{-AB\theta/\pi} & \text{for} \quad 0<\theta<\pi, \qquad (15)\\[2ex] T_w+\dfrac{A}{\beta}\dfrac{1}{e^{AB}-1}+\dfrac{A}{\pi\beta}(\theta-\pi) & \text{for} \quad \pi<\theta<2\pi, \qquad (16)\end{cases}$$

where $A=2\pi R\beta q/rCg$ and $B=h/\beta q$. In this development it is assumed that h is constant throughout the cooled section. Inserting (15) and (16) into the buoyancy integral of (14) leads to expressions in terms of A, B and β. For the apparatus used in this study A was found to be small enough and B was large enough that the

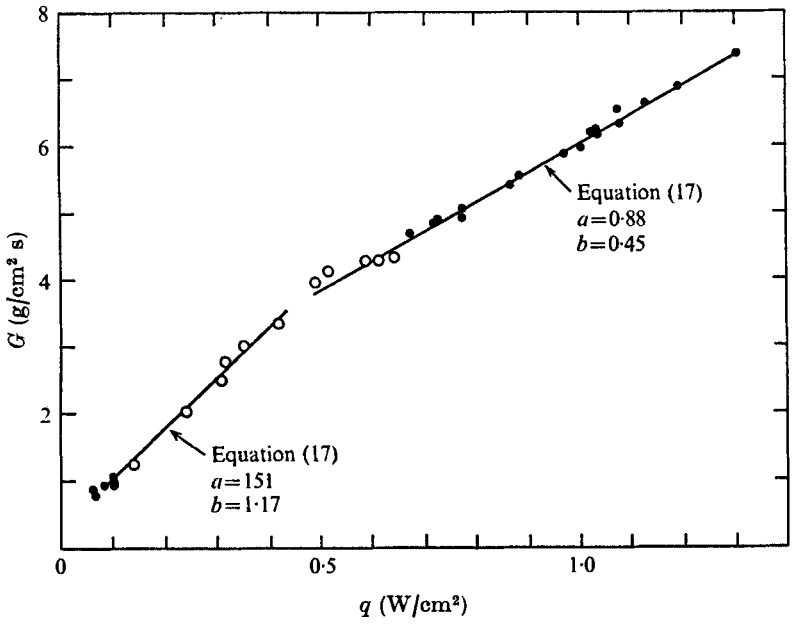

FIGURE 7. Comparison of analytical mass-flux prediction, equation (17), with experiment. ——, analytical prediction. Experiment: ●, stable; ○, unstable.

approximate forms for $A \to 0$ and $B \gg 1$ were sufficiently accurate. On this basis the integral in (14) is approximately $4A/\pi\beta$. Solving for G gives

$$G = [2^{b+2} g R r^b \rho_0^2 \beta q / \pi a C \mu^b]^{1/(3-b)}, \tag{17}$$

or in non-dimensional form,

$$Re^{2-b}/Gr_m = 16/a, \tag{18}$$

where Gr_m is a modified Grashof number defined as $Rg\rho_0^2 r^2 \beta q / \pi \mu^2 GC$. This can also be written as

$$f = 16Gr_m/Re^2 = 4gR\rho_0^2 \beta q / \rho C G^3. \tag{19}$$

Now, f has been determined experimentally as described in § 4 (figure 5), and the resulting correlations are given by (4) and (5). Applying the experimentally determined values of a and b to (17) gives G as a function of q. Figure 7 shows the result for the experimental apparatus. Fluid-property values were evaluated at an average temperature of the water in the loop determined from the thermocouple measurements. The straight-line function approximations were faired through the predicted points. The plotted points, on the other hand, represent the independent experimental determinations of G described in § 4. It can be seen that there is good agreement between theory and experiment. It should be noted, however, that only the experimental points at low and high q were truly representative of steady-state conditions. In the intermediate range the flow was observed to be unstable. The experimental points in that range indicate the time-averaged values of G under oscillatory flow conditions. It is clear that the correlation between the steady-state prediction and experiment is suitable not

only for steady flows, but for the unstable oscillatory flow conditions as well. In view of the fact that the predictions were made using experimentally determined values of a and b, it is not surprising that the measured G values from those same experiments are in good agreement with (17).

According to (10), G is considered independent of θ even under dynamic conditions, provided that the effect of density variations is neglected. In order to investigate the stability of the system, small disturbances are superimposed upon the steady-state conditions, and the dynamics of the system are considered. Thus, following the approach of Welander (1967),

$$G(t) = G_s + G'(t), \tag{20}$$

$$T(\theta, t) = T_s(\theta) + T'(\theta, t), \tag{21}$$

where G_s and T_s represent the steady-state components of the mass flux and temperature, and G' and T' represent small deviations from these values. The flow is stable if these disturbances are damped out, and it is unstable if the disturbances are amplified. In view of the restricted magnitudes of G' and T', no attempt is made to analyse the strongly nonlinear range of large-scale unstable oscillations. Integrating (12) around the loop, as in the steady-state case, and inserting (20) and (21) gives

$$2\pi \frac{dG'}{dt} = -g\rho_0 \int_0^{2\pi} (1 + \beta T_0 - \beta T_s - \beta T') \cos\theta \, d\theta - \frac{a\mu^b [G_s^{2-b} + (2-b) G_s^{1-b} G']}{2^b r^{b+1}} \left(\frac{2\pi}{\rho_0}\right). \tag{22}$$

The two quantities in the square brackets in the last term arise from the linearized expansion for G^{2-b}. Subtracting the steady-state equation (14) from (22) yields the perturbed momentum equation

$$2\pi \frac{dG'}{dt} = g\rho_0 \beta \int_0^{2\pi} T' \cos\theta \, d\theta - \frac{a\mu^b (2-b) G_s^{1-b} G'}{2^b r^{b+1}} \left(\frac{2\pi}{\rho_0}\right). \tag{23}$$

The time-dependent energy equation (11) is treated in a similar manner. Terms of order T' and G' are retained, but second-order terms involving products of these small perturbations are neglected. Subtracting the steady-state energy equation from (11) leads to

$$\frac{CG'}{R} \frac{dT_s}{d\theta} + \frac{CG_s}{R} \frac{\partial T'}{\partial \theta} + \rho_0 C \frac{\partial T'}{\partial t} = \begin{cases} -(2h/r) T' & \text{for} \quad 0 < \theta < \pi, \\ 0 & \text{for} \quad \pi < \theta < 2\pi. \end{cases} \tag{24}$$

In this treatment steady-state correlations are employed for f and h even under dynamic conditions. This is justified, as Welander (1967) has pointed out, when the advection time is large in comparison with the time for momentum or energy to diffuse across the tube cross-section.

For convenience, dimensionless quantities are now defined:

$$\bar{T} = \frac{\beta}{A} T, \quad \bar{t} = \frac{G_s}{R\rho_0} t, \quad \bar{G} = \frac{G}{G_s}.$$

In terms of these new variables and the Laplace operator s, the perturbed momentum equation (23) and energy equation (24) become

$$\frac{2\pi G_s^2}{R\rho_0} s\bar{G}' = g\rho_0 A \int_0^{2\pi} \bar{T}' \cos\theta \, d\theta - \left[\frac{\pi(2-b) a\mu^b G_s^{2-b}}{2^{b-1} r^{b+1} \rho_0}\right] \bar{G}', \tag{25}$$

$$\frac{CG_sA}{R\beta}\frac{d\bar{T}'}{d\theta}+\left(\frac{CG_s}{R}\right)\frac{d\bar{T}_s}{d\theta}\bar{G}'+\left(\frac{CG_sA}{R\rho_0\beta}\right)\rho_0 s\bar{T}'=-\begin{cases}(2hA/r\beta)\bar{T}' & \text{for } 0<\theta<\pi,\\ 0 & \text{for } \pi<\theta<2\pi.\end{cases} \tag{26}$$

G_s and $dT_s/d\theta$ are evaluated from the steady-state solution. Differentiating (15) and (16) and substituting the resulting expressions for $dT_s/d\theta$ into (26) leads to

$$\frac{d\bar{T}'}{d\theta}+\left(s+\frac{AB}{\pi}\right)\bar{T}'+\frac{1}{\pi}\phi(\theta)\bar{G}'=0 \quad \text{for} \quad 0<\theta<\pi, \tag{27}$$

$$\frac{d\bar{T}'}{d\theta}+s\bar{T}'+\frac{1}{\pi}\bar{G}'=0 \quad \text{for} \quad \pi<\theta<2\pi, \tag{28}$$

where $\phi(\theta)$ is defined by

$$\phi(\theta)=AB\exp\frac{AB}{\pi}(\pi-\theta)\Big/(1-e^{AB}). \tag{29}$$

Equations (27) and (28) are linear in $\bar{G}'$ and $\bar{T}'$. Their solutions are

$$\bar{T}'=\begin{cases}\left[K_1-\int\frac{1}{\pi}\phi(\theta)\exp\left\{\int\left(s+\frac{AB}{\pi}\right)d\theta\right\}\bar{G}'\,d\theta\right]\exp\left\{-\int\left(s+\frac{AB}{\pi}\right)d\theta\right\} & \\ \qquad\qquad \text{for} \quad 0<\theta<\pi, & (30)\\ \left[K_2-\int\frac{1}{\pi}\bar{G}'\exp\left(\int s\,d\theta\right)d\theta\right]\exp\left(-\int s\,d\theta\right) \quad \text{for} \quad \pi<\theta<2\pi, & (31)\end{cases}$$

with the boundary conditions based on continuity of temperature,

$$\bar{T}'(s,0)=\bar{T}'(s,2\pi) \quad \text{and} \quad \bar{T}'(s,\pi^-)=\bar{T}'(s,\pi^+).$$

Evaluation of the integrals in (30) and (31) yields

$$\bar{T}'=\begin{cases}K_1\exp\left\{-\left(\frac{D}{\pi}+s\right)\theta\right\}-\bar{G}'\frac{D}{\pi s}\exp\left\{\frac{D}{\pi}(\pi-\theta)\right\}\Big/(1-e^D) \quad \text{for} \quad 0<\theta<\pi, & (32)\\ K_2e^{-s\theta}-\bar{G}'/\pi s \quad \text{for} \quad \pi<\theta<2\pi, & (33)\end{cases}$$

where $D\equiv AB=2\pi Rh/rCG_s$ and where K_1 and K_2 are obtained from the boundary conditions $\bar{T}'(s,0)=\bar{T}'(s,2\pi)$ and $\bar{T}'(s,\pi^-)=\bar{T}'(s,\pi^+)$. Equations (32) and (33) represent the solution to the perturbed energy equation (26), and make it possible to calculate the integral

$$\int_0^{2\pi}\bar{T}'(s,\theta)\cos\theta\,d\theta$$

for substitution into (25). The manipulations are somewhat lengthy, and are therefore not presented in detail here. However, sufficient information has been given so that the interested reader may derive the result, which is

$$\int_0^{2\pi}\bar{T}'\cos\theta\,d\theta=\left\{L+\frac{1}{\pi(e^{-(2\pi s+D)}-1)}\left[\frac{s+D/\pi}{(s+D/\pi)^2+1}(e^{-\pi s-D}+1)(M-e^{-\pi s}N)\right.\right.$$
$$\left.\left.-\frac{s}{s^2+1}(e^{-\pi s}+1)(Me^{-\pi s-D}-N)\right]\right\}\frac{\bar{G}'}{s}, \tag{34}$$

where L, M and N are defined by

$$L=\frac{(D/\pi)^2}{(D/\pi)^2+1}\frac{e^D+1}{e^D-1}, \quad M=1+\frac{De^D}{e^D-1}, \quad N=1+\frac{D}{e^D-1}.$$

For convenience, this result is written as

$$\int_0^{2\pi} \bar{T}' \cos\theta \, d\theta = H(s, D)\, \bar{G}'. \tag{35}$$

Substituting (35) into (25) and rearranging gives

$$\left[H(s, D) - \frac{4(2-b)}{\pi} - \frac{1}{4\pi} \frac{Re^2}{Gr_m} \frac{r}{R} s\right] \bar{G}' = 0. \tag{36}$$

This is written in more compact form as

$$Y(s)\, \bar{G}' = 0, \tag{37}$$

where $Y(s)$ represents the expression in square brackets appearing in (36). In general, s can be taken to be a complex variable such that $Y(s) = Y_r + iY_i$, where Y_r and Y_i are the real and imaginary parts of $Y(s)$.

The stability of the system can be determined by investigating the location of the roots of $Y(s)$. Since $Y(s)$ is a transcendental function there is an infinite number of roots. If all the roots have negative real parts, the corresponding solutions for G' are damped, and the system will return to its steady state after a perturbation. If, on the other hand, any of the roots are in the right half of the s plane (have positive real parts), the corresponding solutions increase in magnitude with time, and the system is therefore unstable. In reality, the flow and temperature deviations from the steady state cannot increase indefinitely in these unstable situations, but they do increase until they are finally limited by the nonlinearity of the actual system.

The Nyquist criterion was used to predict the stability limits. It can be shown that $Y(s)$ has no poles in the right half of the s plane. Equation (34) shows that there are poles at $s = -D/2\pi$ and at $s = -D/\pi \pm i$, a total of three poles, but none of these are in the right half-plane. From a cursory inspection of (34) it appears that there may be poles at the origin and at $s = \pm i$. However, a thorough analysis reveals that there are no poles at these locations since the ratios of the bracketed terms to s^2+1 or s, respectively (which appear as denominators), remain finite in the limit at these three points. The portion of the s-plane contour at infinity maps into a corresponding contour segment at infinity in the left half of the $Y(s)$ plane. Hence, a plot of $Y(i\omega)$ alone reveals whether the origin of the $Y(s)$ plane is encircled. The number of encirclements is equal to the number of roots in the right half of the s plane. One or more roots of this type correspond to instability.

The calculations required to produce detailed contours were somewhat lengthy, but straightforward, and were performed using digital computation. Examples of results of these calculations are plotted in figure 8 for turbulent flow with $D = 0{\cdot}9$ for several values of E, which is defined as $Re^2 r/Gr_m R$. It can be seen from figure 8 that for large values of E, and also for small values of E, the contour does not enclose the origin. Therefore the system is stable in these ranges. For

$$10{\cdot}66 < E < 38{\cdot}38,$$

however, the $Y(s)$ contour encloses the origin, indicating that the system is unstable in this range. On the other hand, similar calculations for large values of D yielded contours which did not enclose the origin for any value of the parameter E.

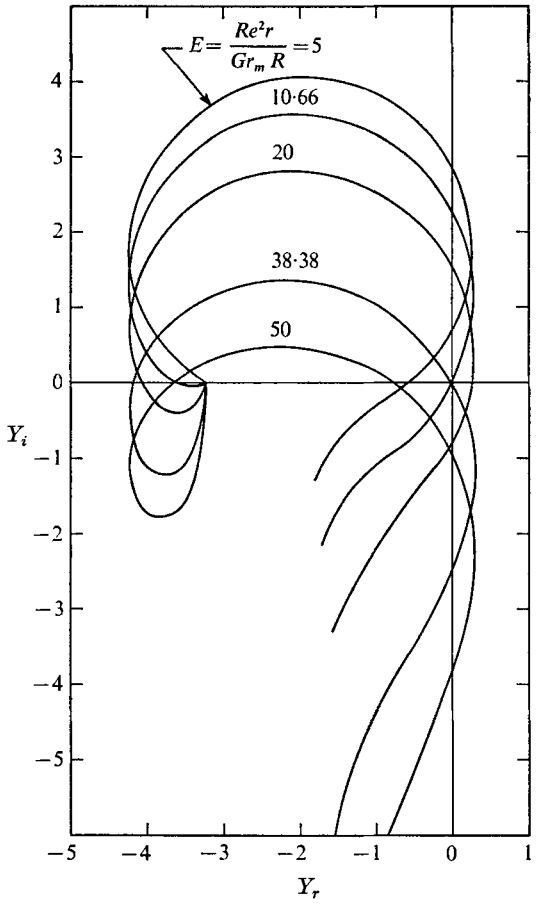

FIGURE 8. Plots of $Y(i\omega)$ for turbulent flow for $D = 0{\cdot}9$.

Hence, for this range of values of D, the corresponding flows were determined to be stable.

Since the stability of the system is determined by the values of D and E, the regions of stability and instability can be illustrated by plotting the boundary between the regions (locus of neutral stability) in D, E co-ordinates. The neutral-stability condition corresponds to the situation where the $Y(i\omega)$ contour passes through the origin of the $Y(s)$ plane (see the contours for $E = 10{\cdot}66$ and $E = 38{\cdot}38$ in figure 8). Thus, points on the stability boundary in the D, E plane are determined by searching for pairs of D and E values for which $Y = Y_r + iY_i = 0$. This occurs when both Y_r and Y_i are zero at some frequency ω, which is unknown at the start of the search procedure. Welander (1967) has developed a similar approach in the determination of neutral-stability conditions.

Since the friction-factor correlation has been established from experiment, b is a known constant. Hence, it can be seen from (36) that Y_r depends only on D and ω, whereas Y_i depends also on E. The fact that Y_r depends on only two parameters, rather than three, is a most fortunate result from the standpoint of the length of the calculations required in the search procedure. The procedure therefore treats

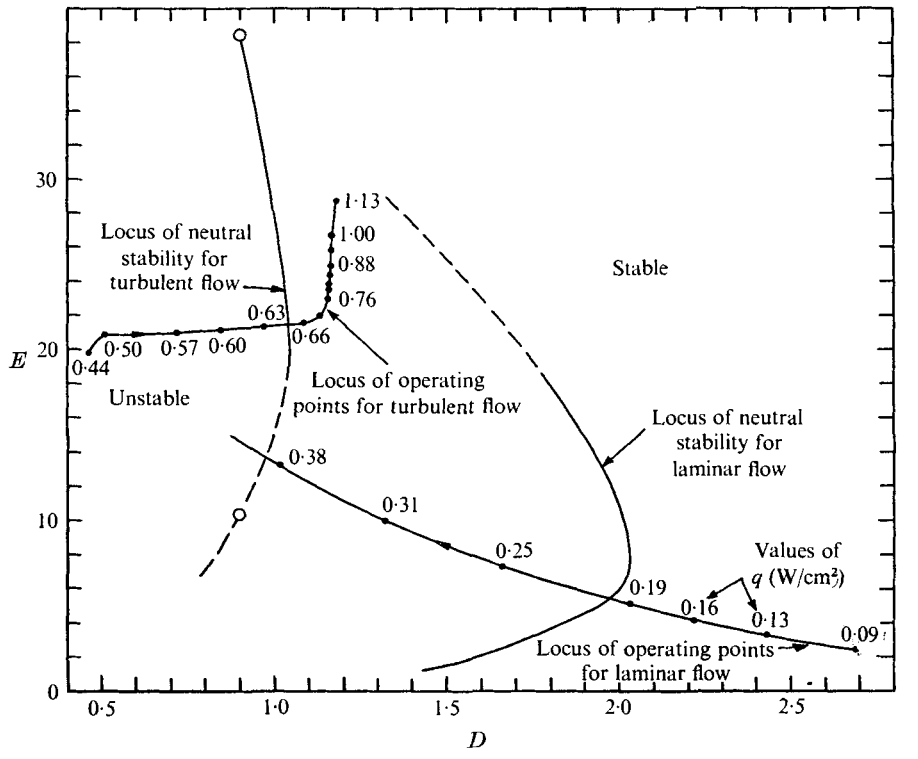

FIGURE 9. Neutral-stability and operating contours.

Y_r first. Initially a value of D is chosen and a search is conducted to find a value of ω which makes $Y_r(D, \omega) = 0$. In some cases no such value of ω is found, indicating that there is no point on the neutral-stability contour for the chosen value of D. In other cases two values of ω which satisfy $Y_r(D, \omega) = 0$ for the positive range of ω are found (see figure 8). These frequencies are denoted by ω_1 and ω_2, respectively, with ω_1 being the lower frequency. Then, two corresponding values of E can be calculated explicitly from $Y_i(D, \omega_1, E) = 0$ and $Y_i(D, \omega_2, E) = 0$. These two calculated values of E are denoted by E_1 and E_2, respectively. For $D = 0{\cdot}9$, for example, $E_1 = 38{\cdot}38$ and $E_2 = 10{\cdot}66$, as shown in figure 8. Thus, for $D = 0{\cdot}9$ there are two points on the neutral-stability contour for turbulent flow, one at $E = 10{\cdot}66$ and the other at $E = 38{\cdot}38$. These are indicated by the two circled points appearing in figure 9. The next step in the procedure is to choose a new value of D and then repeat the process described above. This yields two more points. By establishing pairs of points for each value of D in this manner, the neutral-stability contour for turbulent flow was determined. The laminar flow contour was obtained by exactly the same procedure, except that a different value of b was used. Recall that for laminar flow $b = 1{\cdot}17$ and for turbulent flow $b = 0{\cdot}45$ according to the experiments.

To predict the values of the input heating rate q which result in unstable flows, it is necessary to find the locus of steady-state operating points for the system in the D, E plane, with q as a varying parameter. The intersections of this locus with

System behaviour	Experimentally observed range of q (W/cm^2)	Predicted range of q from figure 9 (W/cm^2)
Stable	0–0·11	0–0·21
Unstable	0·11–0·70	0·21–0·65
Stable	> 0·70	> 0·65

TABLE 1

the neutral-stability contours define the limits of the range of heat inputs corresponding to unstable behaviour (see figure 9).

For the experimental apparatus, a given value of q leads to corresponding calculated values from the steady-state flow analysis. A computed iterative scheme was used to do this in order to obtain an appropriate average temperature for the evaluation of fluid properties. The results of these calculations appear as the locus of operating points in figure 9. Arrows indicate the direction of increasing q. It can be seen from figure 9 that the system is predicted to be stable for q less than 0·21 W/cm^2 and also for q larger than 0·65 W/cm^2, with unstable conditions being predicted for the intermediate range from 0·21 to 0·65 W/cm^2. A comparison with experiment is given in table 1. Considering the complexity of the problem, the above comparison indicates reasonable agreement between experiment and theory as far as ranges of stability and instability are concerned.

The operating contour for laminar flow in figure 9 crosses the neutral-stability contour for turbulent flow when q is slightly above 0·38 W/cm^2. This crossing has no physical significance, however, since the flow is still laminar. Thus, the turbulent neutral-stability contour does not apply to the actual flow and should be disregarded here. For this reason, the turbulent neutral-stability curve is shown as a dashed line rather than a solid line in this region. The same comment applies to the upper portion of the laminar neutral-stability contour, which eventually would be crossed by the operating curve at high values of q.

Oscillation frequencies under unstable conditions were determined from the experimental temperature recordings. These are given in figure 10 as a function of the imposed heat flux. The neutral-stability points from the analysis are also plotted for comparison. The experimental results show that the lowest frequency occurs at the neutral-stability point at the lower heat-flux value. As the imposed heat flux increases from this value, causing the system to move into the unstable region, the observed frequency of oscillation increases monotonically in an approximately linear manner. The highest observed frequency occurs at the neutral-stability point at the higher heat-flux value. Outside the range indicated there are no oscillations since the flow is stable ($0{\cdot}11 > q > 0{\cdot}70$ W/cm^2). The heat flux and frequency at the two neutral-stability points were difficult to determine precisely from experimental observations. In order to demonstrate this difficulty two experimental determinations are shown in figure 10 for each neutral-stability condition. The upper neutral-stability condition exhibits considerable variability. In that case the two heat-flux values deviate from their

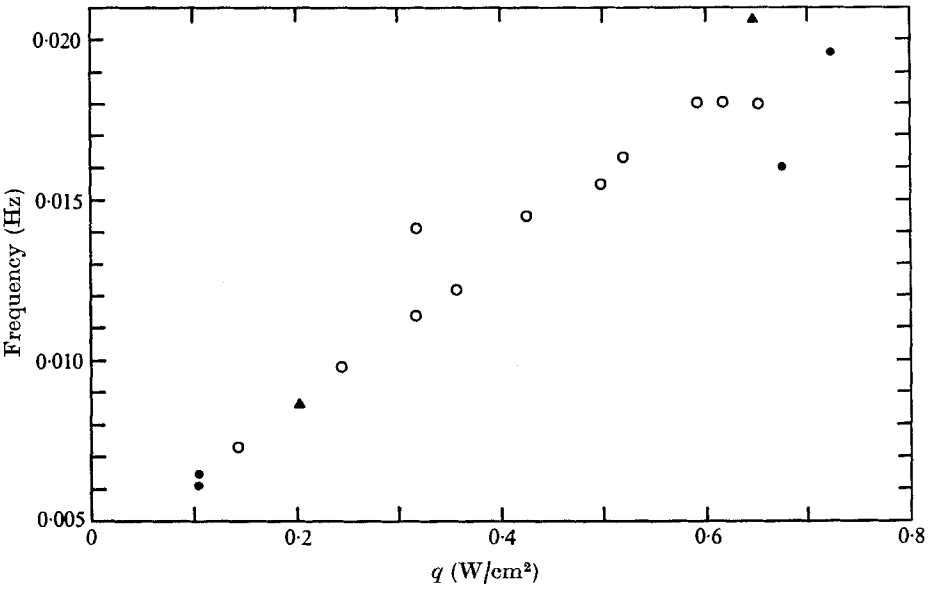

FIGURE 10. Experimentally observed frequency of oscillation as a function of imposed heat flux and comparison with analytically predicted conditions at the two neutral-stability points. Experiment: ○, unstable; ●, neutrally stable. Analytical prediction: ▲, neutrally stable.

mean by about 4 %, while the two frequencies deviate from the mean by approximately 8 %. The analytically determined neutral-stability points appearing in figure 10 occur at frequencies of 0·0086 and 0·0206 Hz. These values deviate from the means of the measured values by 34 % for the lower heat flux and 14 % for the higher heat flux.

Further details of this work are described by Creveling (1964) and de Paz (1972). Sponsorship by the United States Atomic Energy Commission and National Aeronautics and Space Administration are gratefully acknowledged.

REFERENCES

ALSTAD, C. D., ISBIN, H. S., AMUNDSON, N. R. & SILVERS, J. P. 1956 *Argonne Nat. Lab. Rep.* ANL-5409.

CORNELIUS, A. J. 1965 *Argonne Nat. Lab. Rep.* ANL-7032.

CREVELING, H. F. 1964 Ph.D. thesis, Purdue University.

HARDEN, D. G. 1963 *Argonne Nat. Lab. Rep.* ANL-6710.

HOLMAN, J. P. & BOGGS, J. H. 1960 *J. Heat Transfer, Trans. A.S.M.E.* **82**, 221.

KELLER, J. B. 1966 *J. Fluid Mech.* **26**, 599.

PAZ, J. F. DE 1972 Ph.D. thesis, Purdue University.

SCHMIDT, E., ECKERT, E. R. G. & GRIGULL, U. 1939 *Air Material Command, AAF Trans.* no. 527. Wright Field, Dayton, Ohio.

VAN PUTTE, D. A. 1961 M.S. thesis, Purdue University.

WELANDER, P. 1967 *J. Fluid Mech.* **29**, 17.